

# A nanoscale numerical model of calcium silicate hydrate

P.C. Fonseca<sup>a,\*</sup>, H.M. Jennings<sup>b</sup>, J.E. Andrade<sup>c</sup>

<sup>a</sup> Drexel University, Department of Civil, Architectural and Environmental Engineering, Philadelphia, PA, United States

<sup>b</sup> Massachusetts Institute of Technology, Department of Civil and Environmental Engineering, Cambridge, MA, United States

<sup>c</sup> California Institute of Technology, Department of Civil Engineering and Applied Mechanics, Pasadena, CA, United States

## ARTICLE INFO

### Article history:

Received 21 December 2009

Received in revised form 25 April 2011

Available online 31 May 2011

### Keywords:

DEM

Nanoindentation

Microstructure

C–S–H

## ABSTRACT

This manuscript presents a numerical model of the low-density and high-density calcium–silicate–hydrate (C–S–H) gel phases in cement paste. Generated using an autocatalytic growth algorithm, C–S–H is introduced as an assemblage of discrete granular particles at nanoscale with realistic particle-level properties, such as elastic modulus, friction, and cohesion. Using the discrete element method, nanoindentation simulations are performed on each phase, demonstrating that its mechanical contact properties compare well to the results from nanoindentation experiments in the literature. By creating an additional loosely packed phase of C–S–H and maintaining constant particle-level material properties, the results further show that the indentation modulus, as a function of the volumetric packing fraction of the C–S–H gel phase, compares well to a linear self-consistent scaling relation while the hardness most closely fits a nonlinear self-consistent scaling relation.

© 2011 Elsevier Ltd. All rights reserved.

## 1. Introduction

Calcium silicate hydrate (C–S–H)<sup>1</sup> is the primary binding phase in cement-based materials and is the constituent responsible for macroscale cohesion and durability of concrete structures. C–S–H has been described as a gel consisting of separate nanoscale particles with mechanical properties dominated by surface forces (Wittmann, 1976). However, the relationship between this nanostructure and the properties of structural concrete are not fully understood. Models are becoming increasingly important to predict the bulk properties of cement and concrete, such as shrinkage, creep, permeability, and cracking.

C–S–H is responsible for much of the cohesive properties in concrete but the chemical origin of this cohesion is uncertain. Models by Nonat, Jönsson, Pellenq, and colleagues suggest cohesion stems primarily from electro-

static surface charge and, to a lesser extent, from van der Waals forces and capillary tension (Pellenq and Damme, 2004; Jönsson et al., 2004; Nonat, 2004). Although they do not necessarily believe that C–S–H manifests as distinct colloids, their ideas on cohesion are not incompatible with a particulate model. Attractive forces measured by atomic force microscopy (AFM) measure 1 nN forces between surfaces (Lesko et al., 2001, 2004).

Drawing on information from previous models (Jennings and Tennis, 1994) and experimental evidence (Allen et al., 1987), the proposed numerical model for C–S–H is composed of discrete particles each 5 nm in diameter. These particles form two distinct packing densities, known as high-density (HD) and low-density (LD) C–S–H (Jennings, 2000; Tennis and Jennings, 2000; Jennings, 2007). This information makes it possible to analyze C–S–H at a bulk scale using only particle-level information as input. From the following proposed model of C–S–H, indentation properties of the primary binding phase of cement paste will be determined and compared to experimental values in the literature. Using the discrete element method (DEM), nanoindentation simulations on each phase of C–S–H will be performed. By quantitatively comparing these

\* Corresponding author. Tel.: +1 215 571 3786.

E-mail addresses: [fonseca@drexel.edu](mailto:fonseca@drexel.edu), [illa@u.northwestern.edu](mailto:illa@u.northwestern.edu) (P.C. Fonseca), [hjmj@mit.edu](mailto:hjmj@mit.edu) (H.M. Jennings), [jandrade@caltech.edu](mailto:jandrade@caltech.edu) (J.E. Andrade).

<sup>1</sup> Cement chemistry notation: C = CaO, S = SiO<sub>2</sub>, H = H<sub>2</sub>O.

macroscale properties, the model will show that C–S–H behaves like a particulate or discrete material.

## 2. C–S–H particle-level material properties

The elastic properties of C–S–H at the particle scale cannot be probed directly, but instead are deduced from the macroscopic properties of the C–S–H phases. One experimental method by which these particle-level properties are obtained is nanoindentation. In the nanoindentation technique, an indenter with known elastic properties pushes a sample with material properties of interest while the displacement response is recorded. The origin of indentation methods can be traced back to the Mohs' 1822 hardness scale, but the application of this method for determining material properties is credited to Swedish engineer Brinell, who correlated the maximum load and permanent impression of the indenter with the strength of the material. (See Williams (1942) for a historical review). Nanoindentation is simply an indentation test with maximum penetration depth at nanometric length scales rather than micron or millimeter scales. Contact properties such as hardness and indentation modulus can be extracted from these tests. By knowing the volumetric packing fraction of the indented phase, particle-level material properties may be back-calculated from the results. The theory behind the contact problem originates with the 1882 Hertz solution of elastic contact between two spherical surfaces (Hertz, 1882a; Hertz, 1896) and Boussinesq's 1885 and Cerruti's 1882 classical solutions of the stresses and displacements in an elastic half-space (Boussinesq, 1885; Cerruti, 1882).

Because cement paste is a heterogeneous material, a statistical method must be applied to the nanoindentation test so that the mechanical response can be identified for each of the phases. While bulk indentation tests have been performed on cementitious materials as early as the mid 1990s (Kholmyansky et al., 1994; Igarashi et al., 1996; Zhu and Bartos, 1997), to our knowledge, Velez et al. and Acker were the first to differentiate the mechanical properties of individual phases at the micron and nanometric scales. Velez reported the elastic moduli and hardnesses of the four major clinker constituents of Portland cement (Velez et al., 2001), while Acker fine-tuned the test to distinguish between the CH and C–S–H hydration products (Acker, 2001). However, Constantinides et al. were the first to apply a grid indentation and deconvolution technique to capture the elastic properties of two distinct phases of C–S–H (Constantinides, 2005; Constantinides et al., 2003), providing further validation of Jennings' 2000 high-density/low-density model (Jennings, 2000).

Nanoindentation results by Constantinides and Ulm also show that the reduced modulus and indentation hardness of each C–S–H phase is self-consistent (SC) (Constantinides and Ulm, 2007; Ulm et al., 2004). The SC model, originated independently by Hershey (1954) and Kröner (1958), was shown to best capture the microelasticity of materials like C–S–H, where a perfectly disordered solid phase is intermixed with some porosity (Ulm et al., 2007). Caribou et al. show that the indentation hardness has a nonlinear SC scaling relation (Cariou et al., 2008).

Ulm et al. show that for Poisson's ratio  $\nu = 0.2$ , the reduced modulus has a linear SC scaling relation with packing density (Ulm et al., 2007). They also present evidence that both the reduced modulus and hardness have a packing percolation threshold  $\phi_{min} \approx 0.5$ , assuming that the packing fractions of HD and LD phases are 74% and 64%, respectively. These packing densities were determined independently from measured densities of both saturated and dried C–S–H phases (Jennings, 2000). The 50% packing is very close to the theoretical minimum possible stable volume fraction  $\phi_{min} = 0.536$  posed by Song et al. (2008) for granular materials and agrees with the SC model for spherical grains. Finally, the linear SC model for the reduced modulus scales to yield a solid particle modulus at  $\phi_{solid} = 1.0$ . By extrapolating to the solid phase, the solid particle elastic modulus is revealed, providing a material property necessary for quantitatively analyzing a discrete element model.

Both conceptual models and experimental results indicate that C–S–H at the nanometric scale is colloidal, particulate, and discrete. Two phases exist, a high-density and a low-density phase, where  $\phi_{HD} \approx 0.74$  and  $\phi_{LD} \approx 0.64$ . In the proposed model, we predict that particle-level interactions typical of granular materials occur: repulsive forces through normal contact and frictional forces through tangential sliding. Because C–S–H is at the heart of cement cohesion and much of the tensile strength of concrete, these 5 nm particles will include attractive forces that are likely due to electrostatic surface charge and van der Waals forces. By using nanoindentation simulations of a rigid spherical indenter, we will verify self-consistency of the HD and LD C–S–H phases and also compare the reduced modulus and indentation hardness to literature values. The verification of the particle properties will then make it possible to highlight important bulk properties of the C–S–H gel phase.

## 3. C–S–H particle generation

The numerical model is composed of discrete particles that repel each other through contact forces and attract each other through cohesive forces. Although the exact shape of a C–S–H particle is unknown, a monodisperse assembly of spheres was used in the simulation to reduce computational time. The properties of the nanostructure are governed by the magnitude and range of cohesion, elastic properties  $E_p$  and  $\nu$ , particle friction  $\mu$ , and volumetric packing fraction  $\phi$ . Although particle friction has not yet been determined experimentally,  $\mu$  is calibrated against the simulated indentation results for the LD C–S–H phase. By keeping all properties constant and only varying  $\phi$ , the results should predict the indentation hardness and reduced modulus of both C–S–H phases.

The HD phase was generated using a regular assembly of spheres in a hexagonal close packing (HCP) arrangement, where the packing fraction of the HD phase  $\phi_{HD} = \phi_{HCP} \approx 0.7404$ . Although the HD phase does not necessarily have a regular packing, a regular arrangement was chosen because it is the only way to achieve a 0.74 packing fraction using monosized spheres. It is possible that for an HCP arrangement, an unphysical, first order geometrical control may result at 60° planes of weakness that could

further control the resulting failure geometry. However, as shown in Section 5, many of the load-bearing particles in this regular lattice arrangement rearranges below the indenter. This rearrangement helps to break the unrealistic 60° slip-planes.

The LD C–S–H phase was generated using an algorithm to create a random close-packed (RCP) arrangement. This algorithm is based on a theoretical mechanism for cement hydration where particle growth is autocatalytic such that existing particles stimulate the formation of new particles outward from the original nucleation site (Thomas, 2007). A Monte-Carlo algorithm was used to generate an RCP assembly based on this autocatalytic nucleation and growth mechanism. Specifically, a low-resolution particle was placed in the center of a 3-dimensional space. This particle was not a perfect sphere, but it was rotationally symmetric and could pack up to a maximum coordination number of 12. The locations of identical particles were randomly chosen so that new particles touched existing particles. Over 10,000 particles were generated in the simulation. To obtain a constant packing, a cubic representative volume element (RVE) of 6400 particles was chosen from the center. This RVE was then replicated in three dimensions to create approximately 3 million particles.

Using the same coordinates, each particle was then replaced with a sphere each with the same diameter and nearly rigid stiffness. The replacement of the low-resolution particles with perfect spheres initiated some overlap. The particle diameter, which was constant throughout the assembly, was maximized through trial-and-error. Each trial consisted of using Hertz contact forces on overlapping spheres until the system came to equilibrium. The final chosen diameter was the maximum value that allowed for full relaxation in the system, i.e. the maximum diameter that allowed the total stress in the system to approach zero (because there were no longer any overlapping particles). The resulting packing fraction was  $\phi = 0.630$ . This value is very close to analytical ( $\phi = 0.634$ ) and experimental ( $\phi \approx 0.64$ ) calculations of the maximum packing fraction for random close-packed spheres (Song et al., 2008), correlating very closely to a low-density phase of C–S–H.

A third phase was created to yield a random low-packed (RLP) arrangement with an initial  $\phi_{RLP} = 0.550$ . The algorithm to create this RLP phase was the same as that used to generate the LD phase, except that a smaller particle diameter was prescribed for the relaxation stage. The final particle coordinates were scaled so that all particle diameters were 5 nm for both LD and RLP phases. Although there are no experimental tests to directly compare results to the RLP phase, the results from this structure were used to check for consistencies and to compare with a linear self-consistent model for the reduced modulus and a nonlinear self-consistent model for the indentation hardness (Ulm et al., 2007).

#### 4. Simulation method

To test for granular properties of C–S–H, we simulated the nanoindentation of each generated phase of C–S–H with a rigid spherical indenter using the discrete element

method (DEM), a numerical method developed by Cundall and Strack (1979). These simulations were carried out using a modified 2008 build of the Large-scale Atomic/Molecular Massively Parallel Simulator (LAMMPS) developed at Sandia National Laboratories (Plimpton, 1995). Post-processing visualizations were produced using the AtomEye atomistic configuration viewer (Li, 2003).

##### 4.1. Particle forces

Monodispersed spherical particles interacted by Hertzian, history-dependent contact forces and by cohesive forces due to short-range electrostatic surface charge and long-range van der Waals forces. For two contacting spherical particles  $\{i, j\}$  with equal mass and diameter located at positions  $\{\mathbf{r}_i, \mathbf{r}_j\}$ , the particles are in compression such that  $\delta_{ij} = d - r_{ij} > 0$ , where  $d$  is the particle diameter and  $r_{ij} = |\mathbf{r}_{ij}|$  is the distance between particles. The compressive particle force  $\mathbf{F}_c$  is the sum of its normal and tangential components given by Silbert et al. (2001)

$$\mathbf{F}_{nij}(\delta_{ij}) = \sqrt{\delta_{ij}} \left( k_n \delta_{ij} \mathbf{n}_{ij} - \frac{\gamma_n m \mathbf{v}_{nij}}{2} \right) \quad (1)$$

and

$$\mathbf{F}_{sij}(\delta_{ij}) = \sqrt{\delta_{ij}} \left( -k_s \mathbf{u}_{sij} - \frac{\gamma_s m \mathbf{v}_{sij}}{2} \right), \quad (2)$$

where  $\gamma_n$  and  $\gamma_s$  are the normal and tangential damping coefficients,  $m$  is the particle mass,  $\mathbf{n}_{ij} = \mathbf{r}_{ij}/r_{ij}$ , and  $\mathbf{v}_{nij}$  and  $\mathbf{v}_{sij}$  are the relative normal and relative tangential velocities for the particles. The elastic tangential displacement  $\mathbf{u}_{sij}$  is obtained by integrating the tangential relative velocities during elastic deformation while the spheres are in contact. If a local Coulomb yield criterion  $|\mathbf{F}_s| < \mu |\mathbf{F}_n|$  is exceeded,  $\mathbf{F}_{sij}$  is rescaled to have the magnitude  $\mu |\mathbf{F}_n|$  and  $\mathbf{u}_{sij}$  is modified to satisfy Eq. (2).

The normal elastic spring constant  $k_n$  obeys Hertzian normal contact law (Johnson, 1985) such that

$$k_n = \frac{E\sqrt{d}}{3(1 - \nu^2)}, \quad (3)$$

where  $E$  is the Young's modulus and  $\nu$  is the Poisson's ratio of the particle. The tangential spring constant  $k_s$  was tested and reported in Silbert et al. (2001) and Schäfer et al. (1996). The simulations are not very sensitive to the precise value  $k_s/k_n$  and the default value  $k_s/k_n = 2/7$  was chosen so that the period of normal and shear contact oscillations was equal to each other.

The combined modulus  $E_r$ , often referred to as the “reduced modulus” or “indentation modulus,” is related to the material properties of the indented material and the indenter by Johnson (1985)

$$\frac{1}{E_r} = \frac{(1 - \nu^2)}{E} + \frac{(1 - \nu_{ind}^2)}{E_{ind}}, \quad (4)$$

where  $E$  and  $\nu$  are the material properties of the indented material and  $E_{ind}$  and  $\nu_{ind}$  are the material properties of the indenter.  $E_{ind}$  was set arbitrarily high (10,000 GPa) so that the second term in Eq. (4) becomes negligible and the material properties of the material can be related directly by determining  $E_r$  from the simulations. To prevent excessive load relaxation of the indenter, the particle

rotational degree of freedom was blocked. Because C–S–H particles are likely not spherical, this rotational blocking represents a resistance to rolling.

Although the origin of cohesive forces in cement paste is uncertain, we assume that the cohesive force between particles arises from attractive surface charges at short-range distances and van der Waals forces at long-range distances (Pellenq and Damme, 2004; Jönsson et al., 2004; Nonat, 2004). For particles not in contact, the short-range tensile force  $F_{sr}$  was chosen such that  $F_{sr} = -1.5$  nN for  $d < r_{ij} < 1.02d$ .  $F_{sr}$  is an adjustable parameter that compares reasonably well with the approximate 1 nN values measured by atomic force microscopy experiments (Lesko et al., 2001; Plassard et al., 2004).

For  $r_{ij} \geq 1.02d$ , we assume the long-range van der Waals forces  $F_{lr}$  control the tension between particles such that (Hamaker, 1937)

$$F_{lr} = -\frac{A}{6d} \left[ \frac{2(x+1)}{x^2+2x} - \frac{x+1}{(x^2+2x)^2} - \frac{2}{x+1} - \frac{1}{(x+1)^3} \right], \quad (5)$$

where  $A$  is Hamaker's constant and  $x = (r_{ij} - d)/d$ . The Hamaker's constant used in the model is  $10^{-20}$  J, an approximate value suggested by Jönsson et al. (2004) to fall between the values for amorphous silica and mica (Bergström, 1997). To conserve computational resources, a cutoff distance  $r_{ij,max} = 1.1d$  was prescribed at which attractive forces were set to zero. At this particle separation, long-range forces are negligible. Fig. 1 is a plot summarizing the normal particle forces as a function of the particle separation  $r_{ij}$ . Because gravitational forces are several orders of magnitude less than the smallest particle forces, gravity is neglected in the simulations.

#### 4.2. Indentation analysis

One of the primary goals in nanoindentation testing is to calculate the elastic modulus and hardness of a material. These quantities can be accessed using a plot of the load versus penetration depth of the indenter, a plot commonly referred to as the  $P-h$  curve. From the simulations, the force of the indenter  $F_{ind}$  with radius  $R$  is measured at each

desired timestep by summing the forces from each the particles touching the indenter such that

$$F_{ind}(r_a) = \begin{cases} -E_{ind} \sum_{a=1}^{N_c} (r_a - \beta)^2 & r_a < \beta, \\ 0 & r_a \geq \beta, \end{cases} \quad (6)$$

where  $r_a$  is the distance from the center of the particle to the center of the indenter,  $N_c$  is the number of particles in contact with the indenter, and  $\beta = R + d/2$ .

Fig. 2 is a plot of a typical  $P-h$  curve for a nanoindentation simulation where  $P$  is the load and  $h$  is the indentation depth. At the end of the load cycle, the indenter was held stationary to allow for relaxation of the system. The reduced modulus  $E_r$  was then computed from the unloading indentation stiffness  $S$  at the maximum penetration depth  $h_{max}$  such that

$$S = \left. \frac{dP}{dh} \right|_{h=h_{max}}. \quad (7)$$

From (7) we compute  $E_r$  using the Bulyshev–Alekhin–Shorshorov (BASH) equation (Bulychev et al., 1974; Oliver and Pharr, 1992):

$$E_r = \frac{\sqrt{\pi}}{2} \frac{S}{\sqrt{A_c}}, \quad (8)$$

where  $A_c = \pi a^2$  is the projected contact area at the maximum indentation depth. The contact area was determined directly during post-processing by locating the boundary of particles in contact with the indenter at the maximum penetration depth.

The indentation hardness,  $H$ , is the contact pressure of the indenter on the material when the material is fully plastic, defined as

$$H = \frac{P}{A_c}. \quad (9)$$

The contact area used to determine  $E_r$  and  $H$  was computed during post-processing by determining the boundary of particles in contact with the indenter at the onset of unloading. For these simulations, we used a 300 nm indenter radius and indented 40 nm on a simulation box size of

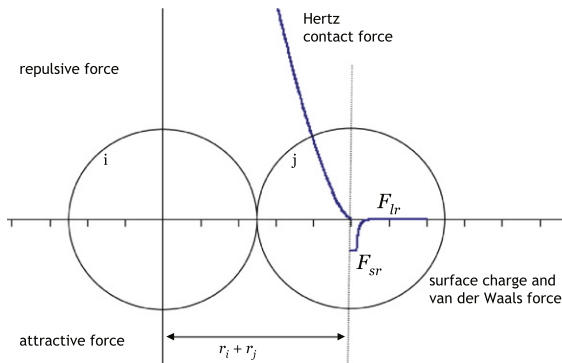


Fig. 1. Combined particle forces as a function of the particle separation  $r_{ij}$  showing compressive Hertz contact force and tensile forces due to short-range surface charge and long-range van der Waals forces.

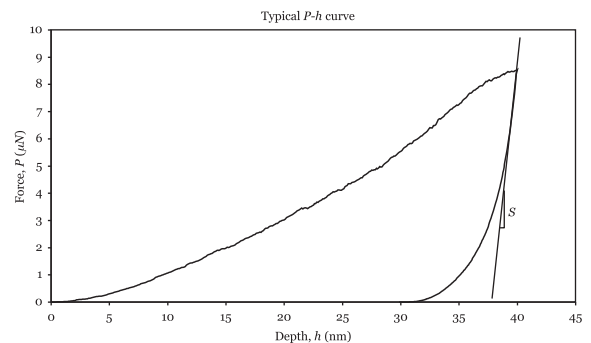


Fig. 2. A sample  $P-h$  curve of loading and unloading of a displacement-controlled nanoindentation simulation with a spherical indenter. The slope  $S = dP/dh$  taken at the onset of unloading is used to compute the reduced modulus  $E_r$ .

approximately  $800 \times 800 \times 500 \text{ nm}^3$  containing over 3 million particles.

#### 4.3. Computation of stresses

For a quasi-static simulation, the stress tensor  $\bar{\sigma}^p$  averaged over a region  $V$  is expressed as (Drescher and de Josselin de Jong, 1972)

$$\bar{\sigma}^p = \frac{1}{V} \sum_{c=1}^{N_c} \mathbf{f}^c \otimes \mathbf{x}^c, \quad (10)$$

where  $\mathbf{f}$  is the discrete force acting at a contact  $c$ ,  $\mathbf{x}^c$  is the position of the point of contact, and  $N_c$  is the number of contacts on the region where the stresses are computed.

The average stresses were computed for each particle in the simulation. Because the shear stiffness and Poisson's ratio of an individual C–S–H particle is uncertain, the deformed particle volume is impossible to calculate with precision. Therefore, each region  $V$  in Eq. (10) is approximated using the undeformed particle volume.

#### 4.4. Other parameters

For these simulations, the particle density  $\rho$  was 2.6 g/cc (Allen et al., 2007). Mass scaling was not employed. Critical global viscous damping, ranging from 0.13  $\mu\text{N}\cdot\text{s}/\text{m}$ –0.16  $\mu\text{N}\cdot\text{s}/\text{m}$ , depended on the particle stiffness and was determined by minimizing the kinetic energy through trial-and-error.

The chosen timestep was  $10^{-12}$  s, determined using (Tu and Andrade, 2008)

$$\Delta t^{\text{crit}} = 2\sqrt{\frac{2m_p}{5k_t}}, \quad (11)$$

where  $m_p$  is the particle mass and

$$k_t = \frac{3(1-\nu)}{2-\nu} k_n \sqrt{\delta_{ij}}. \quad (12)$$

The loading rate, which was selected to minimize dynamic effects, was 10 cm/s. The kinetic energy in the system was monitored to ensure that the simulation remained quasi-static.

The parameters determining the indentation properties of the C–S–H gel are the particle modulus,  $E_p$ , Poisson's ratio,  $\nu$ , magnitude and range of the cohesive forces  $F_{sr}$  and  $F_{lr}$ , packing density,  $\phi$ , and particle friction  $\mu$ . Of these parameters, starting values for  $E_p$ ,  $\nu$ ,  $F_{sr}$ ,  $F_{lr}$ , and  $\phi$  were based primarily on experimental results in the literature. On the other hand, the friction coefficient for an individual C–S–H particle has not been determined directly from experiment. Therefore,  $\mu$  was calibrated against one packing density and was kept constant between phases. Using this method,  $\mu$  was set to 0.65. According to Feiler et al., the friction coefficient between colloids in an aqueous solution range is independent of pH and can range between 0.43 and 0.80 (Feiler et al., 2000). The value  $\mu = 0.65$  for a colloidal C–S–H particle falls in the middle of this range.

Reported values for  $E_p$  range from 48 GPa–65 GPa (Constantinides et al., 2003; Jennings et al., 2007). Simulations

were performed using  $E_p = 48$  GPa,  $E_p = 65$  GPa, and  $E_p = 70$  GPa. Self-consistency was checked by plotting the indentation modulus and hardness versus deformed packing fractions for all three material phases.

## 5. Results

### 5.1. Stresses

Fig. 3(a) and (b) are visualizations of the deviatoric stresses for the random low-packed (RLP) and low-density (LD) C–S–H phases defined by the invariant

$$q = \sqrt{\frac{3}{2}} \|\mathbf{s}\|, \quad (13)$$

where

$$\mathbf{s} = \bar{\sigma}^p - p\mathbf{1} \quad (14)$$

is the deviatoric stress of the stress tensor  $\bar{\sigma}^p$  and  $p\mathbf{1}$  is the volumetric stress tensor.

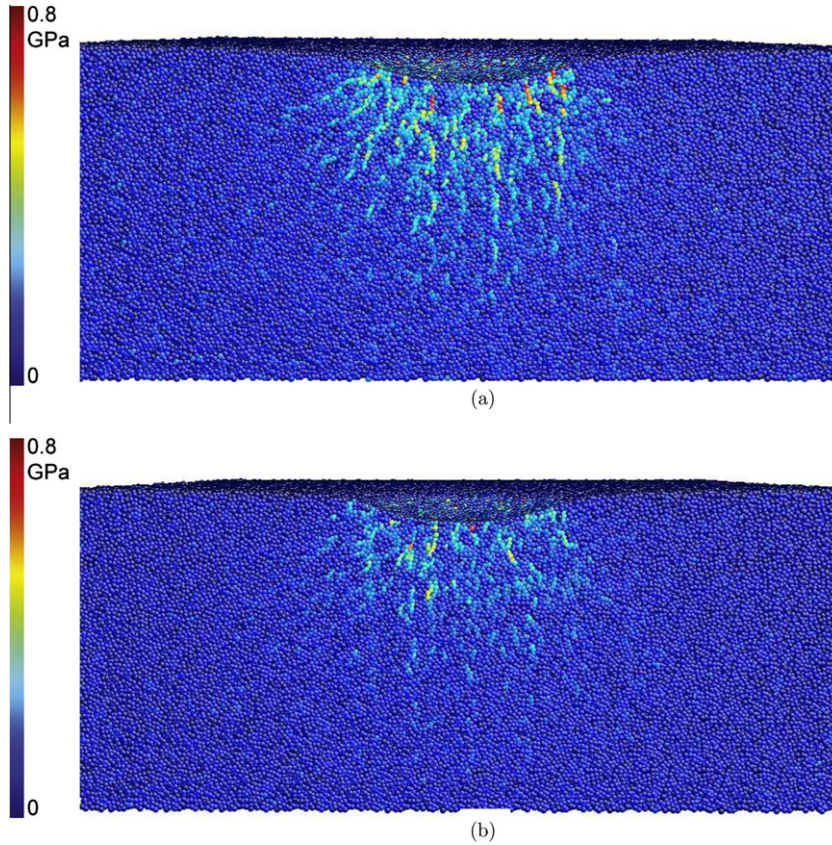
The snapshots were each taken at a section through the center of the indenter coordinates at the maximum penetration depth  $h = 40$  nm. Both the RLP and LD phases carry much of the indenter force through load columns, or force chains, a characteristic typical of jammed granular matter (Cates et al., 1998; Mueth et al., 1998). The maximum deviatoric stress for each of these phases was approximately 0.8 GPa. There were few visible differences between the RLP and LD phases; however, upon further investigation of the post-processing data set, it was clear that the RLP phase contained fewer force chains and fewer total number of compressed particles compared to the LD phase.

Fig. 4 shows  $q$  for the high-density (HD) C–S–H phase. Unlike the LD and RLP phases, there were no visible force chains. Instead, the load more randomly distributed just below the indenter with deviatoric stresses typically ranging from 0.4 GPa to 0.8 GPa.

### 5.2. Packing fractions and coordination numbers of deformed C–S–H

As mentioned in Section 3, the use of a regular hexagonal lattice configuration to represent the HD phase raises a concern that an unphysical geometrical control may occur through  $60^\circ$  planes of weakness in the material. However, as the material deformed, the formation of many of these slip planes were prevented due to particle rearrangement. Fig. 5 shows that the average volumetric packing fractions  $\phi$  and coordination numbers (CN) in a selected volume below the indenter changed after deformation. These changes were most evident in the RLP and HD phases. The HD material (initial packing fraction  $\phi_o = 0.740$ ) dilated below the indenter, creating a final deformed packing fraction  $\phi = 0.714$ . The coordination numbers of the volume below the indenter, all initially 12, randomized such that the material no longer remained assembled as a regular lattice. This rearrangement helped to prevent the unphysical geometrical control from occurring. Fig. 6 shows how the coordination numbers distributed in the deformed LD and HD C–S–H phases.





**Fig. 3.** Visualizations of the deviatoric stresses  $q$  for (a) the low-density (LD) C-S-H and (b) the random low-packed (RLP) material phase. Both materials carried much of the indenter load through force chains with the highest vertical compressive stresses approximately 0.8 GPa. Although the maximum stresses were similar, the LD phase contained more force chains than the RLP phase during indenter loading.

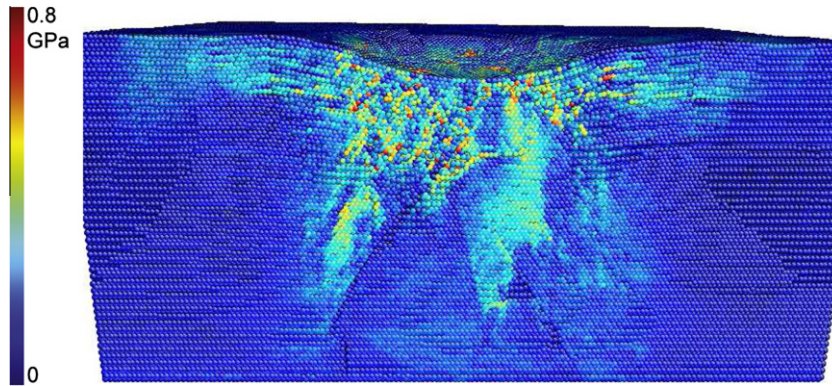


**Fig. 4.** Visualizations of the deviatoric stresses  $q$  for high-density (HD) C-S-H showing no load columns and similar 0.8 GPa maximum stresses compared to the LD and RLP phases.

Unsurprisingly, the LD C-S-H ( $\phi_o = 0.630$ ,  $CN_o = 5.86$ ), which is very close to a random close-packed formation, experienced only a minor increase in both the packing fraction and the coordination number after deformation, with  $\phi = 0.630$  and  $CN = 5.90$ . Furthermore, the RLP material ( $\phi_o = 0.550$ ,  $CN_o = 4.32$ ) consolidated during loading, with  $\phi = 0.569$  and  $CN = 4.60$ .

### 5.3. Indentation properties

We found that the indentation hardness of the material was strongly dependent on values for  $\phi$ ,  $\mu$ , and  $E_p$ . Although  $\mu$  could be increased to more accurately predict experimental hardness measurements, this increase would subsequently lower the reduced modulus  $E_r$  for each pack-

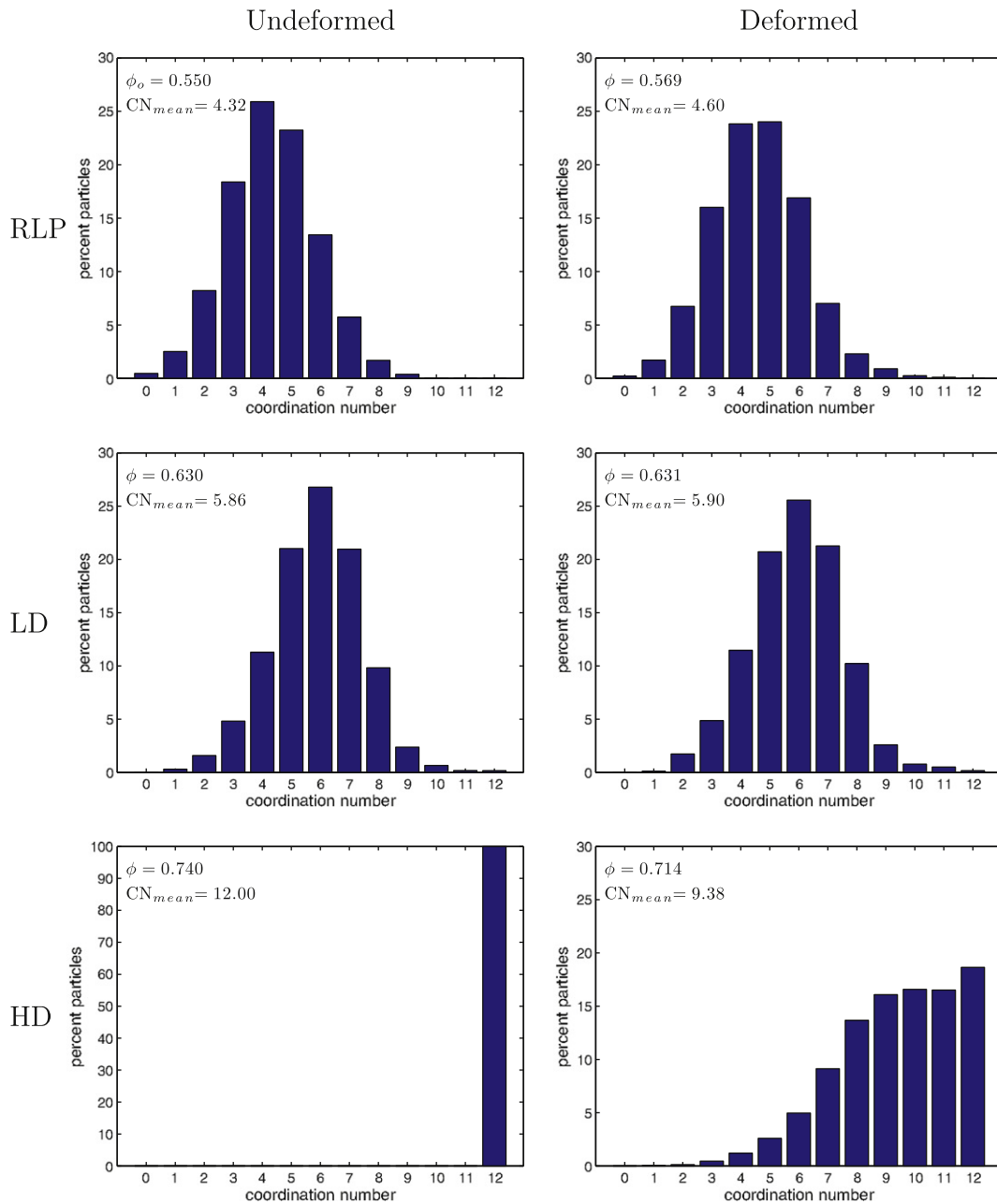
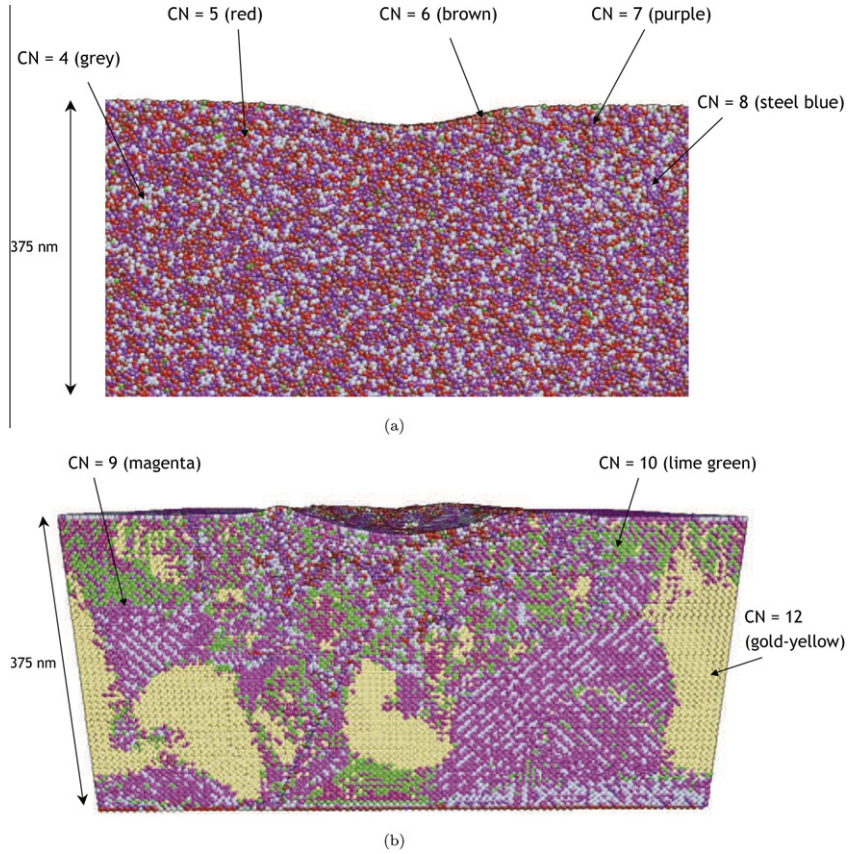


Fig. 5. Histograms of coordination numbers in the region below the indenter for each C–S–H phase before and after the simulated nanoindentation.

ing density. We found that using  $\mu = 0.65$  was the best compromise. This particle friction resulted in a linear self-consistent scaling relation for  $E_r$ , but would result in slightly lower than expected values for the indentation hardness of both LD and HD C–S–H for both  $E_p = 48$  GPa and  $E_p = 65$  GPa. Another option was to raise the particle modulus. For higher particle moduli, (in particular,  $E_p = 87$  GPa), the simulated hardness values closely matched expected values for both LD and HD C–S–H using  $\mu = 0.65$ . However, we felt that  $E_p$  should be based on val-

ues reported in the literature (Constantinides et al., 2003; Jennings et al., 2007) for a more realistic model.

Fig. 7 plots the average hardness results for each particle modulus against the packing fractions of the deformed C–S–H phases. Fig. 7 also compares the results to a nonlinear SC scaling relation for Berkovich and flat-punch indenters. This scaling relation is discussed in detail in Ulm et al. (2007) and Cariou et al. (2008). Figs. 8 and 9 plot  $E_r$  versus deformed packing fractions  $\phi$ . Table 1 lists the hardness calculations for all simulations with comparisons to exper-



**Fig. 6.** Visualizations of the distribution of coordination numbers for the (a) deformed LD C-S-H and the (b) deformed HD C-S-H material phases at the end of the nanoindentation simulation loading cycle. Examples of the coordinations and their respective colors are labeled. The deformed LD material shows that  $CN_{LD}$  is somewhat evenly distributed throughout, with the highest occurrence of CN between 4 and 8. The deformed HD material shows that much of the distribution of CN occurs directly below the indenter, where large regions further from the indenter returned to the initial configuration of  $CN_{HD} = 12$ .

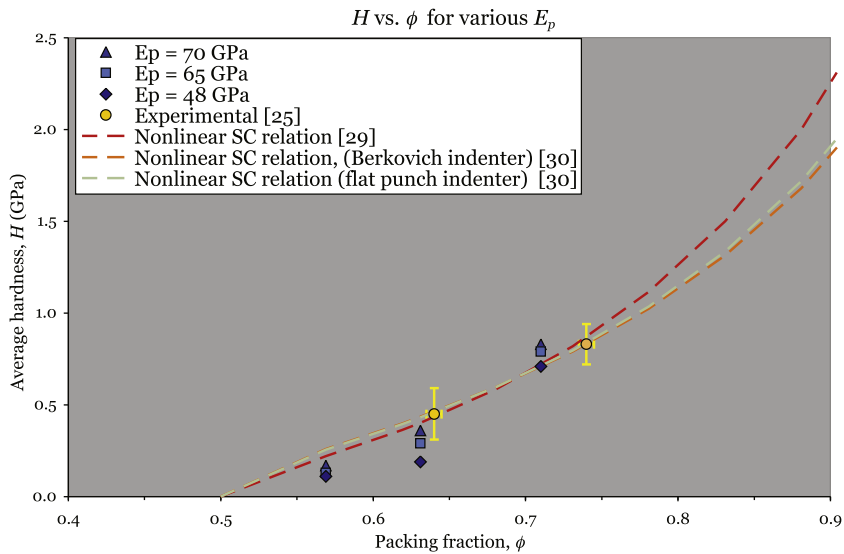


**Fig. 7.** Plot of simulation indentation hardness versus deformed packing fractions  $\phi$  for various particle moduli  $E_p$ . The results are compared to nonlinear SC scaling relations for white cement paste using Berkovich and flat-punch nanoindenters.



imental values. Table 2 lists the average results of  $E_r$  for each particle modulus  $E_p$  and compares to experimental values in the literature. A direct comparison of the simulation results with experimental results should be taken with caution. The simulation results plot hardness and reduced modulus against final deformed packing fractions which are each slightly lower below the LD and HD packing fractions of C–S–H.

## 6. Discussion

Using nanoscale particle-level properties as input, we computed bulk indentation properties for both low-density (LD) and high-density (HD) C–S–H phases using nano-indentation simulations. To test for self-consistency, we also included a random low-packed (RLP) phase. By testing realistic values of the solid elastic modulus  $E_p$ , cohesive

forces  $F_t$ , and calibrating the particle friction  $\mu$  against one C–S–H phase, we determined particle-level properties that resulted in expected values for the bulk indentation properties: the reduced modulus  $E_r$  and the indentation hardness  $H$ . These indentation properties were compared to literature reports from nanoindentation experiments.

Using  $E_p = 65\text{--}70$  GPa,  $\mu = 0.65$ , and maximum  $F_t = -1.5$  nN, the hardness results fell within the range of experimental values (Constantinides and Ulm, 2007) for both LD and HD C–S–H phases. However, the hardness values for the LD and RLP phases fell somewhat below the nonlinear scaling relation developed by Ulm et al. (2007) and Cariou et al. (2008) shown in Fig. 7. Hardness could be increased by simply increasing  $E_p$  or the magnitude of  $F_t$ ; however, an increase in  $E_p$  or  $F_t$  would result in excessively large values of  $E_r$  when compared to experimental values. We also found that  $H$  could be increased with an increase in  $\mu$ , but the result for  $E_r$  would subsequently

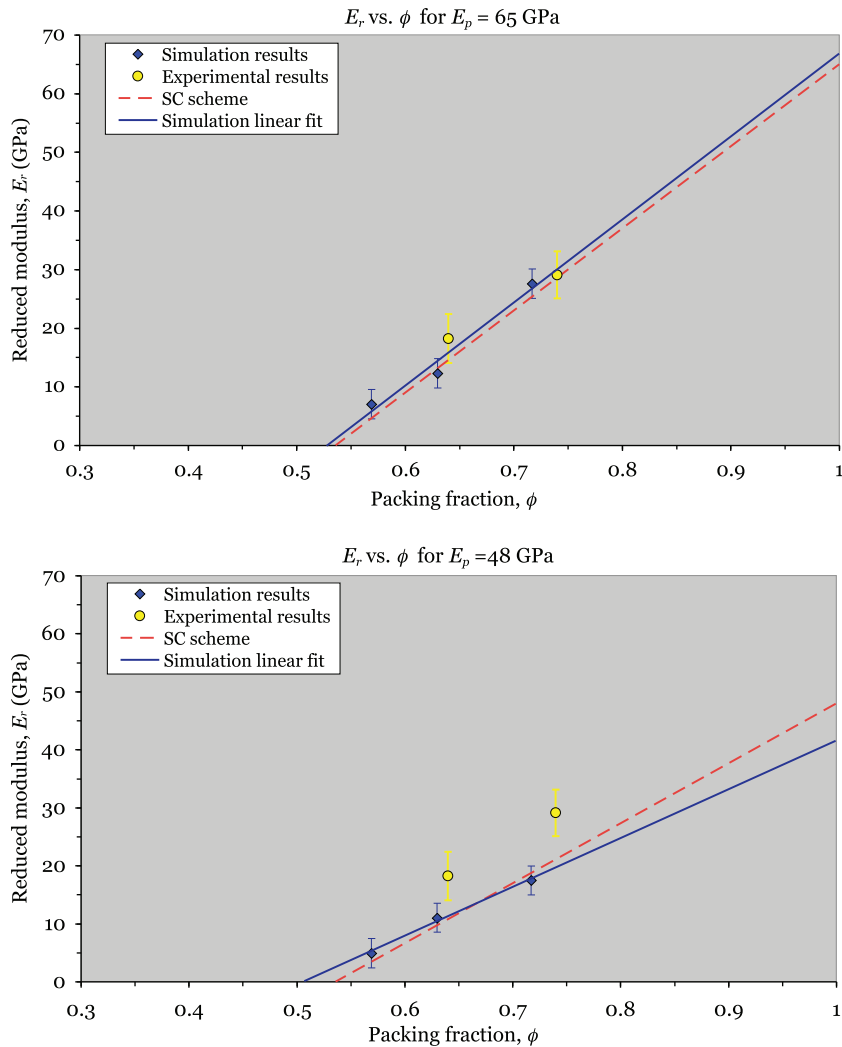


**Fig. 8.** Indentation modulus  $E_r$  at deformed packing fractions  $\phi$  for  $E_p = 65$  GPa and  $E_p = 48$  GPa. The results are plotted with a simulation linear fit and a linear self-consistent scheme for each  $E_p$ , where  $E_r = E_p$  for  $\phi_{solid} = 1.0$  and  $E_r = 0$  for  $\phi_{min} = 0.536$ . Experimental results are taken from Constantinides and Ulm (2007).

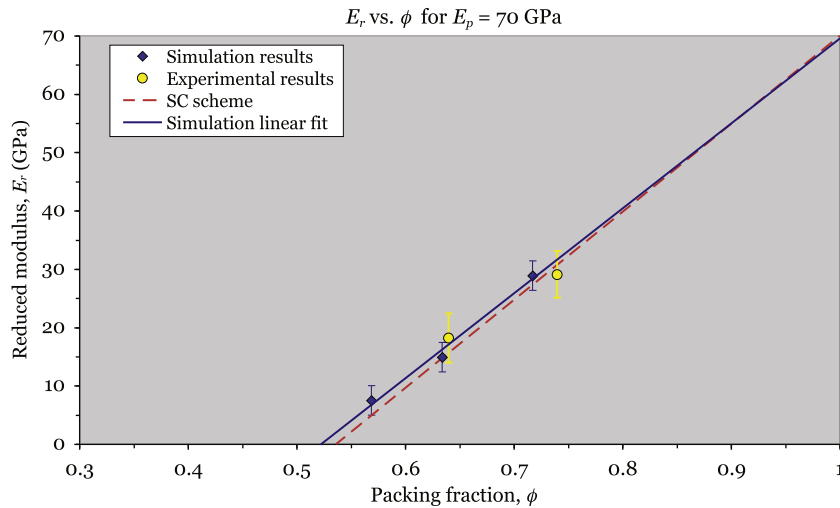


**Fig. 9.** Indentation modulus at deformed packing fractions  $\phi$  for  $E_p = 70$  GPa. The results are plotted with a simulation linear fit and a linear self-consistent scheme, where  $E_r = 70$  GPa for  $\phi_{solid} = 1.0$  and  $E_r = 0$  for  $\phi_{min} = 0.536$ . Experimental results are taken from Constantinides and Ulm (2007).

**Table 1**

Comparison of average simulation hardness values  $H$  to experimental values reported in the literature for HD and LD C–S–H for various particle moduli,  $E_p$ . Reported values for  $E_p$  ranged from 48 GPa–65 GPa.

Type	Experimental (Constantinides and Ulm, 2007)	$E_p = 48$ GPa	$E_p = 65$ GPa	$E_p = 70$ GPa
HD	$0.83 \pm 0.18$	0.71	0.79	0.83
LD	$0.45 \pm 0.14$	0.19	0.29	0.36
RLP	n/a	0.11	0.13	0.17

**Table 2**

Comparison of simulation indentation modulus  $E_r$  to experimental values for various particle moduli  $E_p$ . Note that simulation results are based on deformed packing fractions.

Type	Experimental (Constantinides and Ulm, 2007)	$E_p = 48$ GPa	$E_p = 65$ GPa	$E_p = 70$ GPa
HD	$29.1 \pm 4.0$	$17.5 \pm 2.2$	$27.6 \pm 2.0$	$28.9 \pm 1.9$
LD	$18.2 \pm 4.2$	$11.0 \pm 1.6$	$12.3 \pm 1.6$	$14.9 \pm 1.5$
RLP	n/a	$4.9 \pm 1.4$	$7.0 \pm 1.1$	$7.5 \pm 0.9$

become too low. The reason for this decrease in  $E_r$  with an increase in  $\mu$  is due to fewer permanent particle rearrangements below the indenter during deformation, resulting in a more elastic C–S–H phase.

As shown in Figs. 8 and 9, the reduced modulus compared well with a linear self-consistent (SC) scheme for all deformed packing fractions  $\phi$  and values of  $E_p$  between 65 GPa and 70 GPa such that  $E_r$  scaled from the solid phase ( $\phi_{solid} = 1.0$  at  $E_r = E_p$ ) to a percolation threshold  $\phi_{min} = 0.519 \pm 0.011$  at  $E_r = 0$ . For  $E_p = 48$  GPa, the simulation results did not compare well with the linear SC relation. Using higher stiffness particles ( $E_p = 65$ –70 GPa), the packing density threshold very closely matched both the theoretical lowest stable volume fraction  $\phi_{RLP}^{min} = 0.536$  (Song et al., 2008) and the lowest reported experimental stable volume fraction  $\phi_{RLP} = 0.555 \pm 0.005$  (Onoda and Liniger, 1990) for monodisperse spheres.

The proposed numerical model is expandable to include more complex models with refined capabilities. For example, a discrete model that includes partial or full saturation

will show diminishing van der Waals forces as the disjoining pressure of the water molecules separates the C–S–H surfaces. The result may be that high relative humidities slightly decrease the bulk cohesive properties of the C–S–H gel. The use of non-spherical particles could yield more accurate results, however, this would substantially increase computational time and a lower percolation threshold may then need to be considered for analysis. Alternatively, rotational stiffness could be added to represent the rolling resistance of non-spheres. This rotational stiffness would likely affect the chosen friction coefficient parameter. More advanced models could easily include cement admixtures, such as colloidal nanosilica that should densify the nanostructure. It becomes possible to introduce changes to the nanostructure to predict its effect on cement properties, such as permeability, shrinkage, and creep. This “bottom-up” approach to analyzing the effect of admixtures could play a strong role in redefining how we design new types of cement mixes or repair older cementitious materials.

## 7. Conclusion

A numerical model of the C–S–H gel phases in cement paste was proposed to correlate particle-level properties with bulk indentation properties of high-density (HD) and low-density (LD) C–S–H. These phases consist of discrete assemblies of 5 nm spherical particles with initial undeformed volumetric packing fractions  $\phi_{o,LD} = 0.630$  and  $\phi_{o,HD} = 0.740$ . Using individual particle properties as input, including the particle modulus  $E_p = 65\text{--}70$  GPa, Poisson's ratio  $\nu = 0.2$ , friction  $\mu = 0.65$ , and maximum cohesive tensile force  $F_t = -1.5$  nN, DEM nanoindentation simulations were performed to compare the simulated indentation hardness  $H$  and the reduced modulus  $E_r$  to the self-consistent scaling relation and experimental results in the literature. We found:  $H_{HD} = 0.79\text{--}0.83$  GPa,  $H_{LD} = 0.29\text{--}0.36$  GPa,  $E_{r,HD} = 25.6\text{--}30.8$  GPa, and  $E_{r,LD} = 10.7\text{--}16.4$  GPa for deformed packing fractions  $\phi_{LD} = 0.631$  and  $\phi_{HD} = 0.714$ . The results for  $H$  fell within the range of experimental values but fell slightly below the nonlinear self-consistent scaling relation. The results for  $E_r$  compared well with a linear self-consistent scheme that was plotted against the volumetric packing fractions of the deformed material phases.

A random low-packed material phase with  $\phi_{RLP} = 0.569$  was added to the simulations to further support the evidence that the reduced modulus and hardness of each C–S–H phase is indeed self-consistent. We found that  $E_{r,RLP} = 5.9\text{--}8.4$  GPa which linearly scaled with  $E_{r,LD}$ ,  $E_{r,HD}$ , and  $E_r = E_p$  at  $\phi_{solid} = 1.0$ . The simulation linear fit yielded a percolation threshold  $\phi_{min} = 0.519 \pm 0.011$  at  $E_r = 0$ .

Although the model contains simplifications, such as the use of spheres to represent colloidal C–S–H particles, the results are highly compatible with experimental nanoindentation tests and current theoretical models of C–S–H. Although there may be other realistic particle-level properties, this combination of particle modulus, friction, cohesion, and packing fractions provides a plausible model that results in expected values for indentation hardness and reduced modulus of both LD and HD C–S–H. Nanoscale refinements, such as cement admixtures, could easily be incorporated to analyze its effect on bulk properties. Finally, the results could be upscaled to include other phases of cement paste, such as the clinker phases, calcium hydroxide, and the interfacial transition zone. Using these techniques, we could develop a better understanding of the properties of the C–S–H gel phases and the forces driving the macroscale properties of cement and concrete.

## References

- Acker, P., 2001. Micromechanical analysis of creep and shrinkage mechanisms. In: Ulm, F.-J., Bažant, Z., Wittmann, F. (Eds.), *Creep, Shrinkage and Durability Mechanics of Concrete and other Quasi-Brittle Materials*. Elsevier, pp. 15–26.
- Allen, A.J., Oberthur, R.C., Pearson, D., Schofield, P., Wilding, C.R., 1987. Development of the fine porosity and gel structure of hydrating cement systems. *Philos. Mag.* B 56, 263.
- Allen, A.J., Thomas, J.J., Jennings, H.M., 2007. Composition and density of nanoscale calcium–silicate–hydrate in cement. *Nature* 6.
- Bergström, L., 1997. Hamaker constants of inorganic materials. *Adv. Coll. Int. Sci.* 92, 125–169.
- Boussinesq, J., 1885. *Application des Potentials à l'étude de l'équilibre et du mouvement des solides élastiques*. Gauthier-Villars, Paris.
- Bulychev, S.I., Alekhin, V.P., Shorshorov, M.H., 1974. Mechanical properties of materials studied from kinetic diagrams of load versus depth of impression during microimpression. *Strength Mater.* 8, 1084–1089.
- Cariou, S., Ulm, F.-J., Dormieux, L., 2008. Hardness-packing density scaling relations for cohesive-frictional porous materials. *J. Mech. Phys. Solids* 56, 924–952.
- Cates, M.E., Wittmer, J.P., Bouchaud, J., Claudin, P., 1998. Jamming, force chains, and fragile matter. *Phys. Rev. Lett.* 81, 1841–1844.
- Cerruti, V., 1882. *Ricerche intorno all'equilibrio dei corpi elastici isotropi*. Reale Accademia dei Lincei, Roma, 13.
- Constantinides, G., (2005). *Material invariant properties of cement-based materials: instrumented nanoindentation and microporomechanical modeling*. Ph.D. Thesis, MIT.
- Constantinides, G., Ulm, F.-J., 2007. The nanogranular nature of C–S–H. *J. Mech. Phys. Solids* 55, 64–90.
- Constantinides, G., Ulm, F.-J., van Vliet, K., 2003. On the use of nanoindentation for cementitious materials. *Mater. Struct.* 36, 191–196.
- Cundall, P.A., Strack, O.D.L., 1979. A discrete numerical model for granular assemblies. *Geotechnique* 29.
- Drescher, A., de Josselin de Jong, G., 1972. Photoelastic verification of a mechanical model for the flow of a granular material. *J. Mech. Phys. Solids* 20, 337–340.
- Feiler, A., Larson, I., Jenkins, P., Attard, P., 2000. A quantitative study of interaction forces and friction in aqueous colloidal systems. *Langmuir* 16, 10269–10277.
- Hamaker, H., 1937. The London–Van der Waals attraction between spherical particles. *Physica* IV 10, 1058–1070.
- Hershey, A., 1954. The elasticity of an isotropic aggregate of anisotropic cubic crystals. *J. Appl. Mech.* 21, 236–240.
- Hertz, H., 1882a. Über die Berührung fester elastischer Körper (On the contact of elastic solids). *J. Reine Angew. Math.* 70, 156–171 (For English translation see *Miscellaneous Papers by H. Hertz*, Eds. Jones and Schott, London: Macmillan, 1896.).
- Hertz, H., 1896. Über die Berührung fester elastischer Körper und über die Harte (On the contact of rigid elastic solids and on hardness). In: Hertz, H. (Eds.), *Verhandlungen des Vereins zur Beförderung des Gewerbefleisses*, vol. 61, Leipzig, November 1882b, p. 449 (For English translation see *Miscellaneous Papers by Jones and Schott*, London: Macmillan.).
- Igarashi, S., Bentur, A., Mindess, S., 1996. Characterization of the microstructure and strength of cement paste by microhardness testing. *Adv. Cem. Res.* 8, 877–892.
- Jennings, H.M., 2000. A model for the microstructure of calcium silicate hydrate in cement paste. *Cem. Concr. Res.* 30, 101.
- Jennings, H.M., 2007. Refinements to colloid model of C–S–H in cement: CM-II. *Cem. Concr. Res.* 38, 275–289.
- Jennings, H.M., Tennis, P.D., 1994. Model for the developing microstructure in Portland cement paste. *J. Am. Ceram. Soc.* 77, 3161–3172.
- Jennings, H.M., Thomas, J.J., Gevrenov, J.S., Constantinides, G., Ulm, F.-J., 2007. A multi-technique investigation of the nanoporosity of cement paste. *Cem. Concr. Res.* 37, 329–336.
- Johnson, K.L., 1985. *Contact Mechanics*. Cambridge University Press.
- Jönsson, B., Wennerström, H., Nonat, A., Cabane, B., 2004. Onset of cohesion in cement paste. *Langmuir* 20, 6702–6709.
- Kholmyansky, M., Kogan, E., Kovler, K., 1994. On the hardness determination of fine-grained concrete. *Mater. Struct.* 27, 584–587.
- Kröner, E., 1958. Berechnung der elastischen konstanten des vielkristalls aus den konstanten des einkristalls. *Z. Phys.* 151, 504–518.
- Lesko, S., Lesniewska, E., Nonat, A., Mutin, J.-C., Goudonnet, J.-P., 2001. Investigation by atomic force microscopy of forces at the origin of cement cohesion. *Ultramicroscopy* 86, 11–21.
- Li, J., 2003. AtomEye: an efficient atomistic configuration viewer. *Model. Simul. Mater. Sci. Eng.* 1, 173–177.
- Mueth, D.M., Jaeger, H.M., Nagel, S.R., 1998. Force distribution in a granular medium. *Phys. Rev. E* 57, 3164–3169.
- Nonat, A., 2004. The structure and stoichiometry of C–S–H. *Cem. Concr. Res.* 34, 152–158.
- Oliver, W.C., Pharr, G.M., 1992. An improved technique for determining hardness and elastic modulus using load and displacement sensing indentation experiments. *J. Mater. Res.* 7, 1564–1583.
- Onoda, G.Y., Liniger, E.G., 1990. Random loose packings of uniform spheres and the dilatancy effect. *Phys. Rev. Lett.* 64, 2727–2730.
- Pellenq, R.J.-M., Damme, H.V., 2004. Why does concrete set?: The nature of cohesion forces in hardened cement-based materials. *MRS Bull.*

- Plassard, C., Lesniewska, E., Pochard, I., Nonat, A., 2004. Investigation of the surface structure and elastic properties of calcium silicate hydrates at the nanoscale. *Ultramicroscopy* 100, 331–338.
- Plimpton, S.J., 1995. Fast parallel algorithms for short-range molecular dynamics. *J. Comput. Phys.* 117, 1–19 <<http://lammmps.sandia.gov>>.
- Schäfer, J., Dippel, S., Wolf, D.E., 1996. Force schemes in simulations of granular materials. *J. Phys. I* 6, 5–20.
- Silbert, L.E., Ertas, D., Crest, G.S., Halsey, T.C., Levine, D., Plimpton, S.J., 2001. Granular flow down an inclined plane: Bagnold scaling and rheology. *Phys. Rev. E* 64.
- Song, C., Wang, P., Makse, H.A., 2008. A phase diagram for jammed matter. *Nature* 453, 629–632.
- Tennis, P.D., Jennings, H.M., 2000. A model for two types of calcium silicate hydrate in the microstructure of Portland cement pastes. *Cem. Concr. Res.* 30, 855–863.
- Thomas, J.J., 2007. A new approach to modeling the nucleation and growth kinetics of tricalcium silicate hydration. *J. Am. Ceram. Soc.* 90, 3282–3288.
- Tu, X., Andrade, J.E., 2008. Criteria for static equilibrium in particulate mechanics computations. *Int. J. Numer. Methods Eng.* 75, 1581–1606.
- Ulm, F.-J., Constantinides, G., Heukamp, F.H., 2004. Is concrete a moromechanics material? – A multiscale investigation of poroelastic properties. *Mater. Struct.* 37, 43–58.
- Ulm, F.-J., Vandamme, M., Bobko, C., Ortega, J.A., Tai, K., Ortiz, C., 2007. Statistical indentation techniques for hydrated nanocomposites: concrete, bone, and shale. *J. Am. Ceram. Soc.* 90, 2677–2692.
- Velez, K., Maximilien, S., Damidot, D., Fantozzi, G., Sorrentino, F., 2001. Determination by nanoindentation of elastic modulus and hardness of pure constituents of portland cement clinker. *Cem. Concr. Res.* 31, 555–561.
- Williams, S.R., 1942. *Hardness and Hardness Measurements*. American Society of Metals, Cleveland, Ohio.
- Wittmann, F.H., 1976. The structure of hardened cement paste – A basis for a better understanding of the materials properties. In: *Proceedings of the Conference on Hydraulic Cement Pastes: Their Structure and Properties*, Sheffield. Cement and Concrete Association, p. 96.
- Zhu, W., Bartos, P.J.M., 1997. Assessment of interfacial microstructure and bond properties in aged (GRC) using a novel microindentation method. *Cem. Concr. Res.* 27, 1701–1711.